PHYSICAL REVIEW APPLIED **18,** 044048 (2022)

Tunable Energy-Level Alignment in Multilayers of Carboxylic Acids on Silver

Veronika Stará,[1] Pavel Procházka,[1] Jakub Planer,[1] Azin Shahsavar,[1] Anton O. Makoveev,[1]
Tomáš Skála,[2] Matthias Blatnik,[1] and Jan Čechal[1,3,*]

[1] *CEITEC – Central European Institute of Technology, Brno University of Technology, Purkyňova 123, 612 00 Brno, Czech Republic*

[2] *Department of Surface and Plasma Science, Faculty of Mathematics and Physics, Charles University, V Holešovičkách 2, 180 00 Prague 8, Czech Republic*

[3] *Institute of Physical Engineering, Brno University of Technology, Technická 2896/2, 616 69 Brno, Czech Republic*

(Received 5 May 2022; revised 27 July 2022; accepted 12 September 2022; published 20 October 2022)

Precise energy-level alignment between a metal electrode and an organic semiconductor is required to reduce contact resistance and enhance the efficiency of organic-semiconductor-based devices. Here, we introduce monolayer-thick charge-injection layers (CILs) based on aromatic carboxylic acids that can induce an energy-level shift in subsequent layers by up to 0.8 eV. Through a gradual chemical transformation of the as-deposited molecules, we achieve a highly tunable energy-level shift in the range of 0.5 eV. We reveal that the work function and energy-level positions in the CIL increase linearly with the density of induced dipoles. The energy-level position of subsequent layers follows the changes in the CIL. Our results thus connect the energy-alignment quantities, and the high tunability would allow precise tuning of the active layers deposited on the CIL, which marks a path towards efficient charge-injection layers on metal electrodes.

DOI: 10.1103/PhysRevApplied.18.044048

I. INTRODUCTION

Organic electronics gained a significant position in illumination and display technologies [1–3], with other areas employing organic semiconductors (OSCs), i.e., organic thin-film transistors [4], and organic photovoltaics [5] being on the edge of large-scale industrial application. To utilize OSCs as active components in fast switching electrical devices, forming good electrical contact is essential [6–9]. The interface between the OSC active layer and the metallic contacts defines the charge-injection efficiency of the device, e.g., the alignment of the molecular-orbital levels of the organic layer with the vacuum and Fermi levels of the metal electrodes determines electron and hole injection, and a considerable contact resistance arises from their misalignment [7,10–12]. The high contact resistance limits the operation frequency and restricts high current devices, such as organic field-effect transistors [7,8].

The introduction of ordered dipolar layers at the metal-OSC interface can effectively tune the electrode's work function (WF) and interfacial energy-level alignment (ELA) and, correspondingly, the charge-carrier injection barriers into adsorbate layers [13]. Passivation of the metal electrode by a thin insulating layer can establish the ELA through integer charge transfer via the tunneling barrier [14,15]. However, the tunneling contact is associated with considerable contact resistance and energy losses, despite the precise alignment [16]. Hence, the direct contact of molecules with the electrode surface is preferable. In this case, the deposited molecules can form interfacial dipolar layers and act as so-called charge-injection layers (CILs) that reduce the energy-level misalignment, thus increasing the efficiency of OSC-based devices [17,18]. The dipoles within CILs can be either intrinsic to the adsorbed molecules or form due to the chemical interaction of the adsorbed molecules with the substrate, molecule-substrate charge transfer, or changing the molecular conformation (e.g., its bending) and orientation with respect to the surface [13].

Extensive surface-science studies provide a fundamental understanding of the role of dipolar layers in the changes of WF and ELA, as demonstrated for many molecular systems [10,13,19,20]. However, only some molecular systems provide the possibility of ELA tuning, e.g., by precoverage [21], bicomponent blending [22], or electric field tuning in disordered layers [23]. Recently, a high tunability of the electrode's WF was demonstrated by changing the composition at the dielectric-metal interface of the epitaxial MgO layer on the Ag surface [24], but the tunneling barrier still featured a considerable contact resistance. Precise tunability by a homogeneous single-component molecular layer would provide a significant advantage for

---

[*] cechal@fme.vutbr.cz

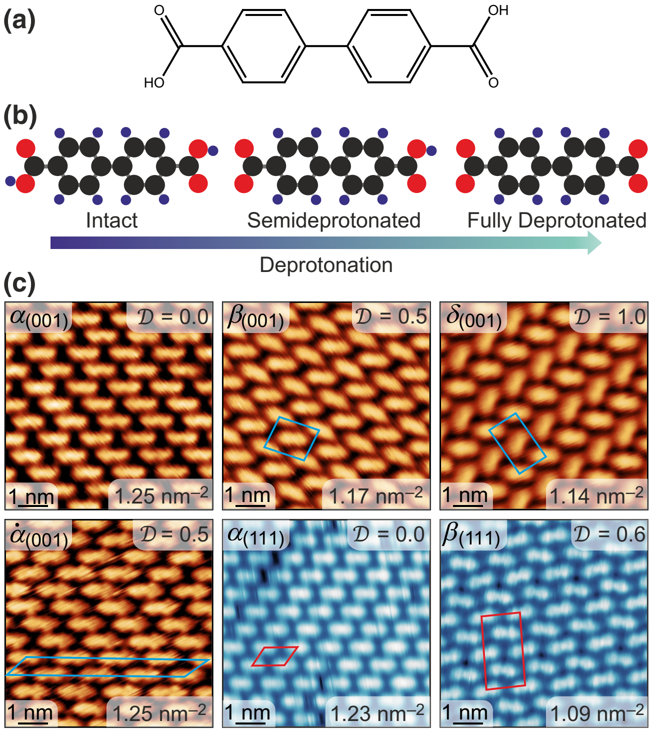

FIG. 1. Molecule and CILs employed in this study. (a) Chemical structure of BDA. (b) Partially and fully deprotonated BDA has a similar structure but largely differing properties compared to intact BDA. (c) STM images of distinct CILs considered in this study. Degree of deprotonation, $\mathcal{D}$, is given for each phase. Quadrangles mark the BDA unit cells (note that there is no unit cell for the $\alpha_{(001)}$ phase). Density of BDA molecules, n_{BDA} per nm^2, of every CIL is given in the bottom-right corner.

the fabrication of low-contact-resistance interfaces. In this respect, a recent theoretical study introduced the possibility of tuning the work function in the range of 1 eV by changing between electron-donor and -acceptor character through on-surface chemical interconversion of deposited molecules [25]. Following this concept, we employ 4,4′-biphenyl dicarboxylic acid [BDA, Fig. 1(a)] to prepare a range of single-layer molecular CILs with a tunable density of interface dipoles that are formed by the chemical transformation of the BDA molecules in direct contact with the metal substrate. The formed electrical dipoles induce energy shifts of molecular layers by up to 0.8 eV. We establish a linear relationship between the WF change and the electrostatic shift in the C 1s position within the first molecular layer (referred to as the CIL) and the second molecular layer. Finally, we present a continuous tuning of WF and ELA by a gradual deprotonation of BDA.

II. METHODS

A. Experimental details

Both the CIL and subsequent layers are deposited under ultrahigh vacuum (UHV) conditions (base pressure below 2×10^{-10} mbar) on the surfaces of Ag(001) and Ag(111) single crystals, which are first cleaned by repeated cycles of Ar$^+$ sputtering and annealing at 520 °C. All analyses are performed under UHV conditions without exposing the sample to the ambient environment. We employ synchrotron-radiation photoelectron spectroscopy [26] as the primary tool to determine the electronic properties of the CILs; the measurements are performed at the Materials Science Beamline at the Elettra synchrotron light source in Trieste. Overall, the experimental details are the same as those reported previously [27]. In brief, we use 40.8-, 420-, 510-, and 670-eV excitation energies to measure the valence band, C 1s, Ag 3$d_{5/2}$, and O 1s spectra, respectively. Detailed spectra are acquired in the medium-area lens mode using 10-eV pass energy integrating 3 (Ag 3d, C 1s) or 25 (O 1s) sweeps with 0.1-s dwell time and 0.05-eV energy steps. The total resolution is in the range of 300–550 meV. The peak positions are corrected with respect to the measured Fermi edge of the Ag substrate, and the intensity is normalized to the photocurrent of a gold mesh placed in the beamline. In addition, we apply a −7-V bias to the sample during secondary-electron cutoff (SEC) measurements, and, subsequently, we shift the spectra according to the measured Fermi-level position, setting it to 0.00 eV.

The synchrotron measurements are combined with laboratory measurements in which we develop methodologies to prepare the CILs by UHV deposition and subsequent thermal annealing [27–30]. We employ low-energy electron microscopy (LEEM) to assess the coverage, low-energy electron diffraction (LEED) and scanning tunneling microscopy (STM) to determine the structure, and x-ray photoelectron spectroscopy (XPS) to measure the chemical composition and electronic properties of the samples; the exact experimental parameters were detailed previously [27–30]. X-ray-induced deprotonation is followed in real time by XPS on the samples kept at 25 °C. A nonmonochromatized Mg $K\alpha$ x-ray source operating at 300-W power is positioned about 25 mm from the sample surface, which corresponds to about 8×10^{10} photons/s, according to the manufacturer.

B. Theoretical approaches

All calculations are based on density-functional theory (DFT) and performed using the Vienna *ab initio* simulation package [31]. The projector-augmented wave (PAW) [32] method is employed to treat the core electrons. For silver, oxygen, hydrogen, and carbon, 11 valence electrons ($5s^1 4d^{10}$), 6 valence electrons ($2s^2 2p^4$), 1 valence electron ($1s^1$), and 4 valence electrons ($2s^2 2p^2$), respectively, are expanded in a plane-wave basis set with an energy cutoff set to 450 eV. The Brillouin zone is sampled with a Γ-centered Monkhorst-Pack grid [33], using more than 17 k-points per Å^{-1} for all the structural relaxations and

60 k-points per Å^{-1} for the subsequent electronic structure calculations. Ionic relaxations are stopped when all the residual forces become smaller than 4×10^{-2} eV/Å. In all the calculations, total energy, potential, and forces are corrected for finite-size errors. All the slabs consist of eight layers with lateral cell dimensions corresponding to the optimized silver bulk lattice constants. For the $\alpha_{(001)}$, $\dot{\alpha}_{(001)}$, and $\delta_{(001)}$ phases, the BDA molecular layers are adapted to the silver (001) supercell with matrix notations $\begin{pmatrix} 3 & 2 \\ -2 & 2 \end{pmatrix}$ for the α and $\dot{\alpha}$ phases and $\begin{pmatrix} 3 & 5 \\ -3 & 2 \end{pmatrix}$ for the δ phase. All slabs are separated by a vacuum gap of 18 Å. We use the nonlocal optB88-vdW DFT functional [34] to describe the exchange-correlation energy. Benchmark calculations using PBE-D3 [35] and optB86b-vdW [36] functionals show no qualitative differences in the evaluated dipole moments.

III. RESULTS AND DISCUSSION

A. Linear relationship between work function and core-level shifts in the CIL

1. BDA molecular phases on silver substrates

The BDA molecule features two phenyl rings that impose its flat-lying geometry on metal surfaces and two carboxyl ($-$COOH) end groups that mediate intermolecular hydrogen bonding and enable the formation of extended supramolecular assemblies. BDA molecules in direct contact with the silver substrate chemically transform when annealed at elevated temperatures—their carboxyl groups deprotonate, i.e., lose hydrogen [Fig. 1(b)] [37]. Hence, we obtain three chemically distinct molecular species with similar structures. After removing hydrogen, the resulting carboxylate group possesses a partial negative charge, which leads to a formation of an interfacial dipole and the rearrangement of molecules into a structurally distinct phase. Through gradual deprotonation, we can prepare a range of molecular phases with a distinct density of dipoles n_{dip}. Here, we consider six distinct stable BDA molecular phases as CILs: the α, $\dot{\alpha}$, β, and δ phases [27,28,30] on Ag(001) and the α and β phases on Ag(111) [29]; the STM images of these phases are given in Fig. 1(c). In the following, we designate the full monolayers of these phases as CILs and denote them by the Greek letter representing the molecular phase with the orientation of the surface plane in the index, e.g., $\beta_{(001)}$ stands for the β phase on the Ag(001) surface.

These phases differ in the degree of deprotonation, $\mathcal{D}$, of carboxyl groups of BDA molecules. We define degree of deprotonation as the ratio of deprotonated to the total number of carboxyl groups. The values of $\mathcal{D}$ determined by fitting the O 1s XPS spectra are given in the particular STM images in Fig. 1(c) for all the considered phases. The measured spectra of the $\alpha_{(001)}$ and $\dot{\alpha}_{(001)}$ CILs are given in Fig. 2. The O 1s spectrum of the $\alpha_{(001)}$ CIL in Fig. 2(c) shows two peaks: the one at a binding energy (BE) of 534.05 eV is associated with hydroxyl $(\mathrm{C}-\underline{\mathrm{O}}\,\mathrm{H})$ and the one at 532.65 eV with carbonyl $(\mathrm{C}=\underline{\mathrm{O}}\ )$ oxygens of the carboxyl groups. Upon thermal annealing of the $\alpha_{(001)}$ CIL to 70 °C, half of the carboxyl groups deprotonate and the $\dot{\alpha}_{(001)}$ CIL is formed [27]. The O 1s spectrum significantly changes: there is one dominant component at 530.9 eV associated with carboxylate oxygens $(-\mathrm{C}\underline{\mathrm{O}}\,\underline{\mathrm{O}}^{\,-})$ and two peaks at 532.8 and 531.45 of the two oxygen atoms of the carboxyl group bound to carboxylate [dark red peaks in Fig. 2(d)] [27,28]. The spectra measured for the other CILs are provided in the Supplemental Material, Secs. 1 and 2 [38]. From the fitted spectra, $\mathcal{D}$ is determined as the ratio of the intensity of peaks associated with the deprotonated carboxyl groups to the total intensity of the O 1s peak.

The deprotonated carboxyl groups are associated with a dipole moment: the density of dipoles, n_{dip}, therefore increases with $\mathcal{D}$. For each molecular phase, n_{dip} is obtained as $n_{\mathrm{dip}} = 2\mathcal{D}n_{\mathrm{BDA}}$, where n_{BDA} is the surface density of BDA molecules in the particular phase; the factor 2 reflects two carboxyl groups per BDA. The densities, n_{BDA}, are determined from the unit cells established by the local congruence method from low-energy electron diffractograms [27–30]; the n_{BDA} values are provided in the STM images given in Fig. 1(c). For the considered CILs, n_{dip} ranges from 0 ($\alpha_{(001)}$, $\alpha_{(111)}$), 1.17 ($\beta_{(001)}$), 1.25 ($\dot{\alpha}_{(001)}$), and 1.30 dipoles per nm^2 ($\beta_{(111)}$) to 2.28 dipoles per nm^2 ($\delta_{(001)}$).

The C 1s spectrum of the $\alpha_{(001)}$ CIL [Fig. 2(a)] shows the main component at 285.25 eV; it is associated with the C atoms of the phenyl rings. The carboxylic C 1s component is shifted by 4.4 eV to higher BE; the remaining features are associated with an extensive shake-up satellite structure [39,40]. The presence of the extensive shake-up satellite structure complicates the precise fitting of carboxyl-related components, as discussed previously for BDA on the Ag(111) substrate [41]. Therefore, we do not consider the position of carboxyl-group-related components when discussing the CIL properties. As carbon atoms do not chemically interact with the substrate (see below), we employ the C 1s level position to describe electrostatic core-level shifts and ELA of the second BDA layer.

2. Change of work function during the thermal-induced transformation

Upon deposition of the molecular layer and during its transformation, the sample's WF significantly changes. We determine the WF for all considered CILs and bare substrates by employing a standard procedure of measuring the SEC and Fermi levels [10,42,43], as demonstrated in Fig. 2(e) for the $\alpha_{(001)}$ and $\dot{\alpha}_{(001)}$ CILs; all the measured SEC are given in Fig. S6 within the Supplemental Material,

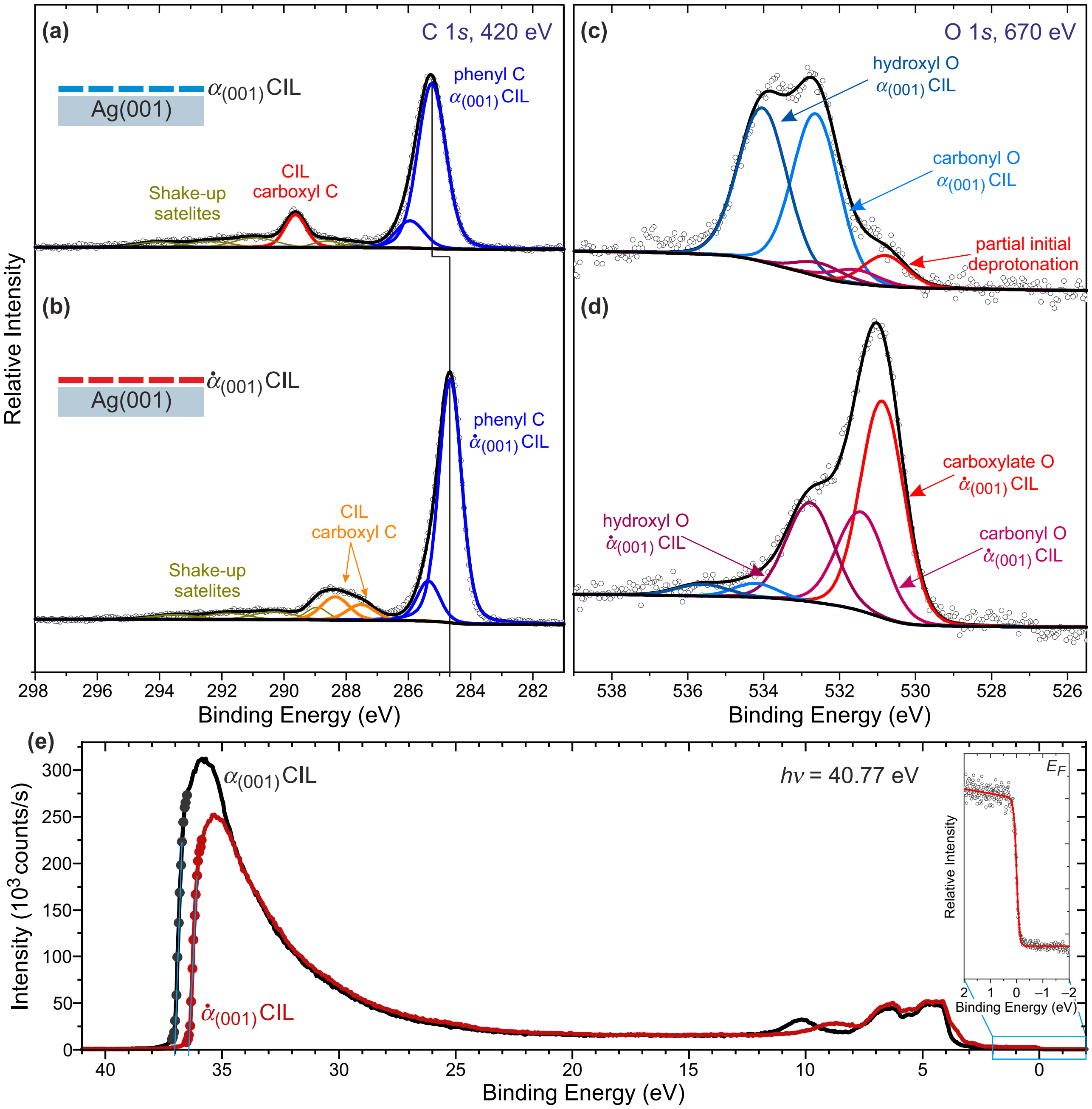

FIG. 2. Photoelectron-spectroscopy analysis of the BDA CILs. (a), (b) C 1*s* spectra measured by synchrotron radiation with an energy of 420 eV from samples comprising a full layer of BDA deposited on Ag(001) substrates, that is, $\alpha_{(001)}$ and $\dot{\alpha}_{(001)}$ CILs. Peak components are marked by the associated chemical states; the full description and peak parameters for all CILs are given in the Supplemental Material, Secs. 1 and 2 [38]. Vertical lines mark the shift of the peaks discussed in the text. (c), (d) O 1*s* spectra (670 eV) of $\alpha_{(001)}$ and $\dot{\alpha}_{(001)}$ CILs. (e) Wide spectra and details of the Fermi edge measured on samples with $\alpha_{(001)}$ and $\dot{\alpha}_{(001)}$ CILs used for the determination of the WF. Full data for all CILs are given in the Supplemental Material, Sec. 3 [38].

Sec. 3 [38]. For the as-deposited molecular layers, the WF significantly decreases, but with the temperature-induced deprotonation of the carboxyl groups [Fig. 3(a)], the WF increases [Fig. 3(b)]. The WF increases linearly with $\mathcal{D}$, but the slope changes when $\mathcal{D} = 0.5$ is reached. To gain a deeper understanding of these changes, we perform DFT calculations for the $\alpha_{(001)}$, $\dot{\alpha}_{(001)}$, and $\delta_{(001)}$ phases.

3. DFT calculations of a dipole moment in the $\alpha_{(001)}$, $\dot{\alpha}_{(001)}$, and $\delta_{(001)}$ phases

The dipole moment for each phase is calculated for the $\alpha_{(001)}$, $\dot{\alpha}_{(001)}$, and $\delta_{(001)}$ phases [Figs. 4(a)–4(c)] as the sum of interface (μ_{int}) and intramolecular (μ_{mol}) dipole moments. The interface dipole moments contain a contribution from the push-back effect and a contribution

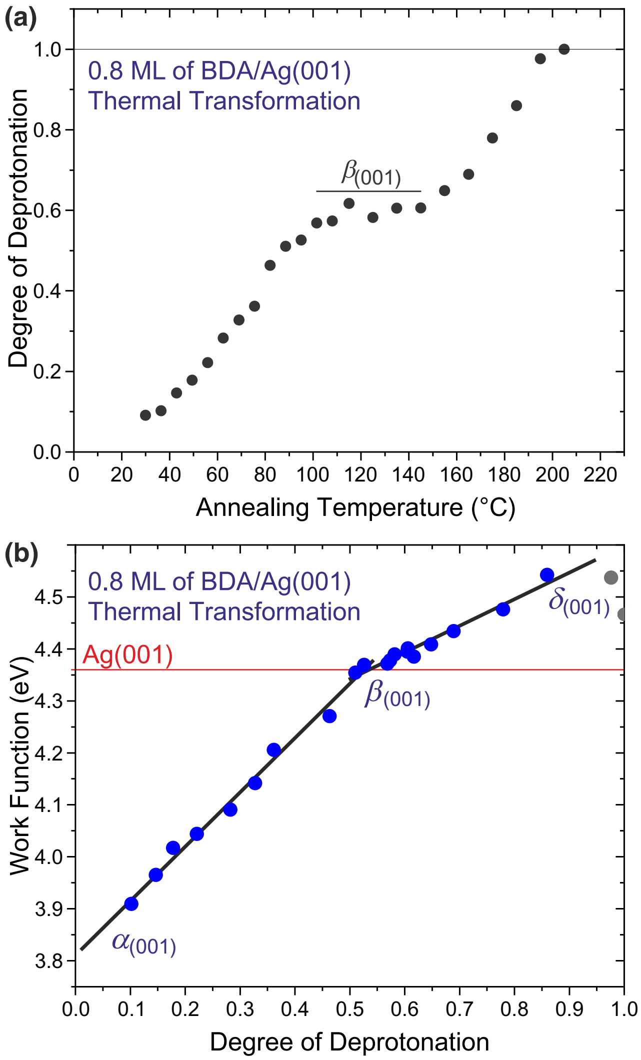

FIG. 3. (a) Degree of deprotonation of carboxyl groups obtained during gradual annealing of the sample with 0.8 monolayer (ML) of BDA on Ag(001) up to 200 °C. After each annealing step, heating is turned off and the spectra are measured. Black line indicates the temperatures at which the degree of the deprotonation only slightly changes with temperature; we associate this region with the $\beta_{(001)}$ phase. (b) Change of work function as a function of the degree of deprotonation. Red horizontal line marks the measured substrate work function (4.36 eV). Two last points are given in gray as there is a loss of BDA molecules due to desorption.

TABLE I. Calculated dipole moments and work-function changes for the $\alpha_{(001)}$, $\dot{\alpha}_{(001)}$, and $\delta_{(001)}$ phases. The calculated dipole moments for the $\delta_{(001)}$ phase are normalized to the size of the $\alpha_{(001)}$ supercell.

Phase	μ_{int} (D)	μ_{mol} (D)	μ_{tot} (D)	$e\Delta\varphi$ (eV)
$\alpha_{(001)}$	−1.16	−0.05	−1.21	−0.53
$\dot{\alpha}_{(001)}$	0.98	−1.01	−0.03	−0.04
$\delta_{(001)}$	2.98	−2.20	0.78	0.33

from the interface dipoles induced by charge transfer. The μ_{mol} term contains a dipole moment localized within the molecular layer. It is induced by the bending of BDA molecules [see Figs. 4(g)–4(i)] due to a strong interaction of the deprotonated carboxylic groups with the silver substrate. Absolute values of the interface dipole moments are calculated from the electron-density difference ($\Delta\rho$) between the silver substrate and the molecular layer, which is defined as

$$\Delta\rho = \rho_{\mathrm{BDA+Ag}} - (\rho_{\mathrm{BDA}} + \rho_{\mathrm{Ag}}), \tag{1}$$

where $\rho_{\mathrm{BDA+Ag}}$ is the total electron density of the combined system, ρ_{Ag} marks the electron density of the silver substrate without the molecular layer, and ρ_{BDA} is the electron density of a free-standing BDA monolayer. The expression for the interface dipole moments is

$$\mu_{\mathrm{int}} = \iiint z\Delta\rho(x,y,z)dxdydz. \tag{2}$$

The intramolecular part of the dipole moment is calculated from the total charge density of the molecular layer, including the ionic contribution:

$$\mu_{\mathrm{mol}} = \iiint z\rho_{\mathrm{BDA}}dxdydz - \sum_{i}^{N} Z_i q_i, \tag{3}$$

where N, Z_i, and q_i denote the number of ions in the molecular layer, their positions, and charges, respectively. The resulting dipole moment, i.e., $\mu_{\mathrm{tot}} = \mu_{\mathrm{int}} + \mu_{\mathrm{mol}}$, is in perfect agreement (less than 0.06 D in absolute values) with its evaluation from the work-function change [44]. Calculated interface, intramolecular, and total dipole moments for the $\alpha_{(001)}$, $\dot{\alpha}_{(001)}$, and $\delta_{(001)}$ phases are listed in Table I.

Charge transfer between the substrate and the molecular layer can be defined as the maximum absolute value of the cumulative charge-transfer function, $Q(z)$ [45]. This function represents the total charge transferred below an (001) plane at position z:

$$Q(z) = \iint \int_{-\infty}^{z} \Delta\rho(x,y,z)dxdydz. \tag{4}$$

The optimized structures, averaged electron-density differences after adsorption, and electronic charge-transfer functions for the $\alpha_{(001)}$, $\dot{\alpha}_{(001)}$, and $\delta_{(001)}$ phases are depicted in Fig. 4. As shown in Fig. 4(d), about 0.1 electrons from the $\alpha_{(001)}$ phase are transferred to the silver substrate, which induces an interface dipole moment of $\mu_{\mathrm{int}} = -1.16$ D while the molecule stays planar, and we observe only a small contribution from the intramolecular dipole

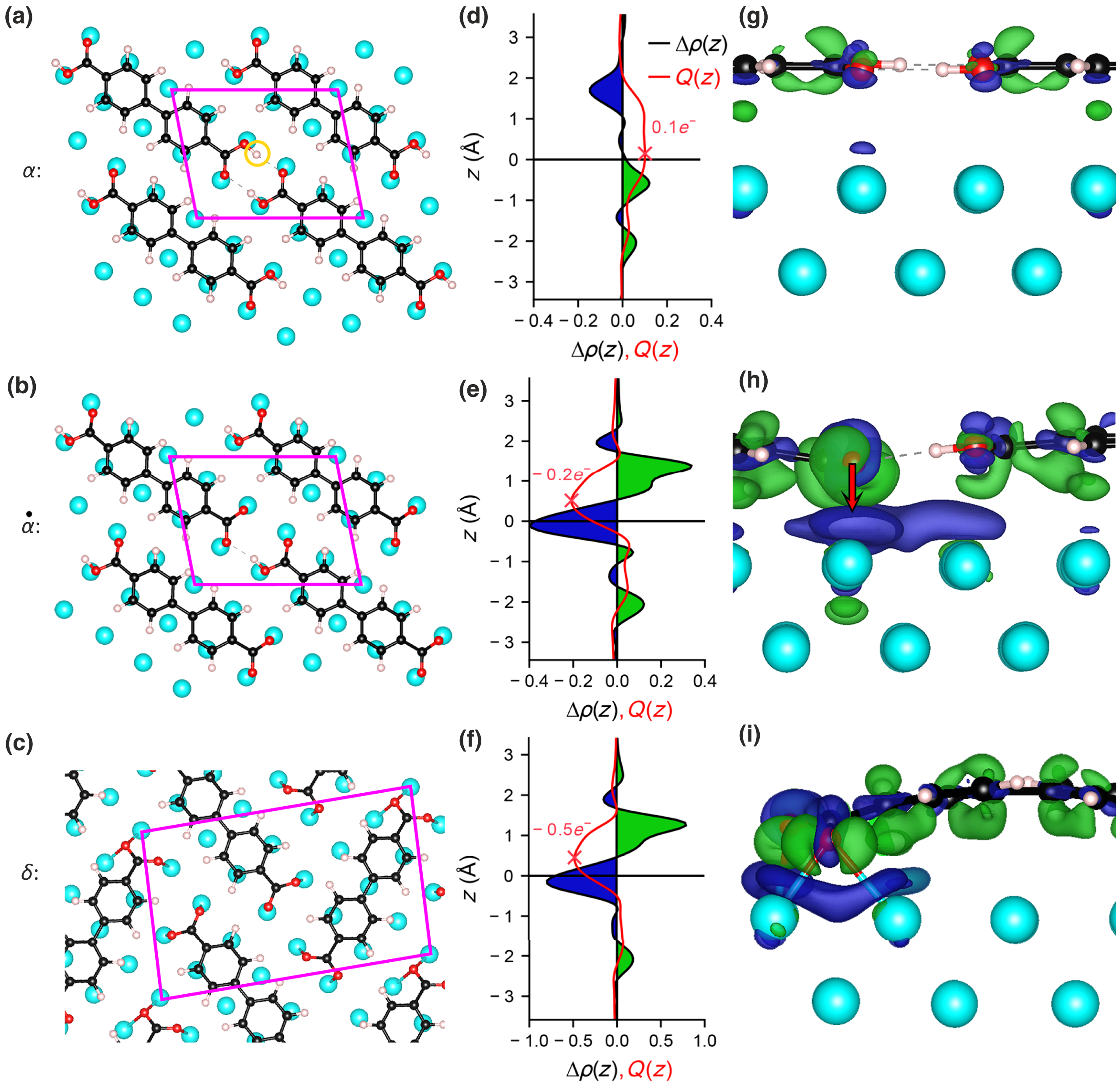

FIG. 4. (a)–(c) Calculated unit cells for the α, $\dot{\alpha}$, and δ phases. Cyan, black, red, and white spheres represent Ag, C, O, and H atoms, respectively. The orange circle marks an extra hydrogen atom in the α phase. (d)–(f) Averaged electron-density difference over the x-y plane and charge-transfer functions for the α, $\dot{\alpha}$, and δ phases, respectively. Black horizontal line represents the calculated center of a dipole [see Eq. (3)]. (g)–(i) Charge-density redistribution in the α, $\dot{\alpha}$, and δ phases, respectively, induced by the interaction between the silver substrate and the molecular layer. Red arrow marks the shift of the deprotonated carboxylic group towards the silver substrate.

moment, $\mu_{\mathrm{mol}} = -0.05$ D; the total dipole moment is -1.21 D. After deprotonation of the $\alpha_{(001)}$ phase, i.e., removal of the hydrogen atom marked in Fig. 4(a) and transformation to the $\dot{\alpha}_{(001)}$ phase [Fig. 4(b)], the molecular system undergoes qualitative changes in both the structure and electronic configuration. The deprotonated carboxylic group is pushed towards the silver substrate, which causes a bending of BDA molecules [Figs. 4(g) and 4(h)]. This is accompanied by two effects: first, about 0.2 e^- are transferred from the silver substrate to the molecular layer [Fig. 4(e)], which changes the interface dipole moment to $\mu_{\mathrm{int}} =$ 0.98 D. Second, the intramolecular dipole moment is decreased to $\mu_{\mathrm{mol}} = -1.01$ D due to the out-of-plane deviation of negatively charged oxygen atoms, see Table I. Hence, the total dipole moment in the $\dot{\alpha}_{(001)}$ phase is -0.03 D, i.e., it is increased by 1.17 D with respect to the $\alpha_{(001)}$ phase. After the full deprotonation of BDA molecules and transformation to the

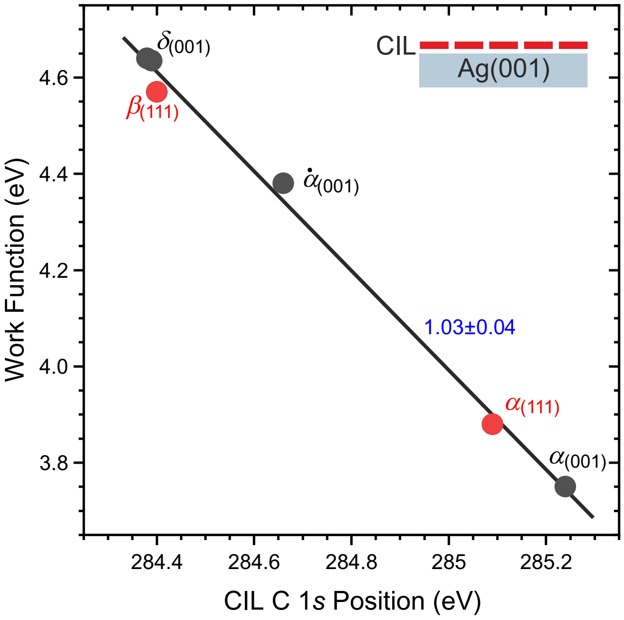

FIG. 5. Dependence of work function on the position of the C 1*s* component associated with the phenyl rings for the BDA CILs marked at each point.

$\delta_{(001)}$ phase [Fig. 4(c)], both contributions to the resulting dipole moment and charge-transfer functions follow the same trend. First, charge transfer from the silver substrate increases to about 0.5 e^- [Fig. 4(f)], which also increases the interface dipole moment to $\mu_{\text{int}} = 2.98$ D. Second, the BDA molecules undergo even more prominent bending [Fig. 4(i)], which is accompanied by an additional decrease of the intramolecular dipole moment to $\mu_{\text{mol}} = -2.20$ D. As a result, the total dipole moment is increased by 0.82 D with respect to the $\dot{\alpha}_{(001)}$ phase to 0.79 D. This change is smaller, by 30%, than the one observed during the transformation of the $\alpha_{(001)}$ phase to the $\dot{\alpha}_{(001)}$ phase due to a smaller increase of the interface dipole moment by 0.14 D and a larger decrease of the intramolecular dipole moment by 0.23 D. This is consistent with the work-function measurements as a function of the degree of deprotonation, showing a gentler slope during the transformation of $\alpha_{(001)}$ into the $\beta_{(001)}$ phase [Fig. 3(b)]. Finally, the resulting changes in the calculated work function (Table I) are in perfect agreement with experiments (cf. Fig. 6): they differ by 0.08, 0.06, and 0.05 eV for the $\alpha_{(001)}$, $\dot{\alpha}_{(001)}$, and $\delta_{(001)}$ phases, respectively.

4. Discussion of the relationship between work function and core-level shifts in the CIL

During the thermal treatment of a BDA submonolayer, we establish that the work function increases linearly with the degree of deprotonation of BDA's carboxyl groups, as detailed above. The linear dependence can also be established between the position of the CIL C 1*s* peak and the measured WF of the full molecular layer, as given in Fig. 5. On the surface of a metal, the change of the work function, $e\Delta\varphi$, is induced by the formation of molecular dipoles, $e\Delta\varphi_{\text{dip}}$ [44]:

$$e\Delta\varphi = e\Delta\varphi_{\text{dip}}. \tag{5}$$

The term $e\Delta\varphi_{\text{dip}}$ comprises contributions from the interface and intramolecular dipoles. The deposited molecules induce interfacial charge redistribution (push-back effect) that decreases the work function [10,11,46,47], whereas the deprotonated carboxyl groups display a negative charge localized on the O atoms [27,41], which results in a WF increase [48–51]. There are two contributions to the formed dipoles revealed by our DFT calculations: the interface dipoles increase the WF, whereas the intramolecular dipoles formed due to the BDA molecule bending decrease the WF. Our experiments show that the $\alpha_{(001)}$ CIL displays a work function 0.61 eV lower than the Ag(001) substrate, the $\dot{\alpha}_{(001)}$ CIL's work function is similar to that of the substrate (0.02 eV higher), and the $\delta_{(001)}$ CIL has a WF 0.28 eV higher than that of the bare Ag(001) substrate, consistent with our DFT calculations. In line with the WF change, the core energy levels of BDA molecules shift accordingly as the dipoles electrostatically induce shifts in the kinetic energies of the photoelectrons [13]. Our observation is consistent with studies on OSC bilayers, in which the local electrostatic potential of formed interface dipoles is identified as the origin of the change in molecular-orbital energies [22,52].

B. Energy-level alignment in BDA bilayers

Figures 6(a)–6(d) show the photoelectron spectra of the second BDA layer deposited on the $\alpha_{(001)}$ and $\dot{\alpha}_{(001)}$ CILs. The spectra of the respective CILs are given in Fig. 2, and the complete set of spectra is provided in the Supplemental Material, Secs. 1 and 2 [38]. After deposition of the second layer of BDA, the photoelectron spectra are more complex [Fig. 6(c)]. For their fitting, we introduce two additional peaks with BEs of 534.2 and 532.8 eV and a 1:1 ratio of intensities that represent the α phase in the second BDA layer. For the CIL (i.e., the first layer), we use the previously obtained peak positions, Gaussian widths, and intensity ratios and allow only a change in the peak intensity. Peaks with the same separation and intensity ratio also appear in the spectra of the second BDA layer on top of $\dot{\alpha}_{(001)}$ [Fig. 6(d)] but are shifted to lower BEs (533.7 and 532.30 eV). The presence of well-defined peaks associated with the protonated carboxyl groups suggests that the second-layer BDA molecules are intact, i.e., nondeprotonated. The intact BDA molecules in the second layer are also found for all other CILs in this study. No deprotonation in the second layer is observed, even on the $\delta_{(001)}$ CIL, which features only deprotonated BDA molecules, even after annealing at elevated temperatures. The second BDA

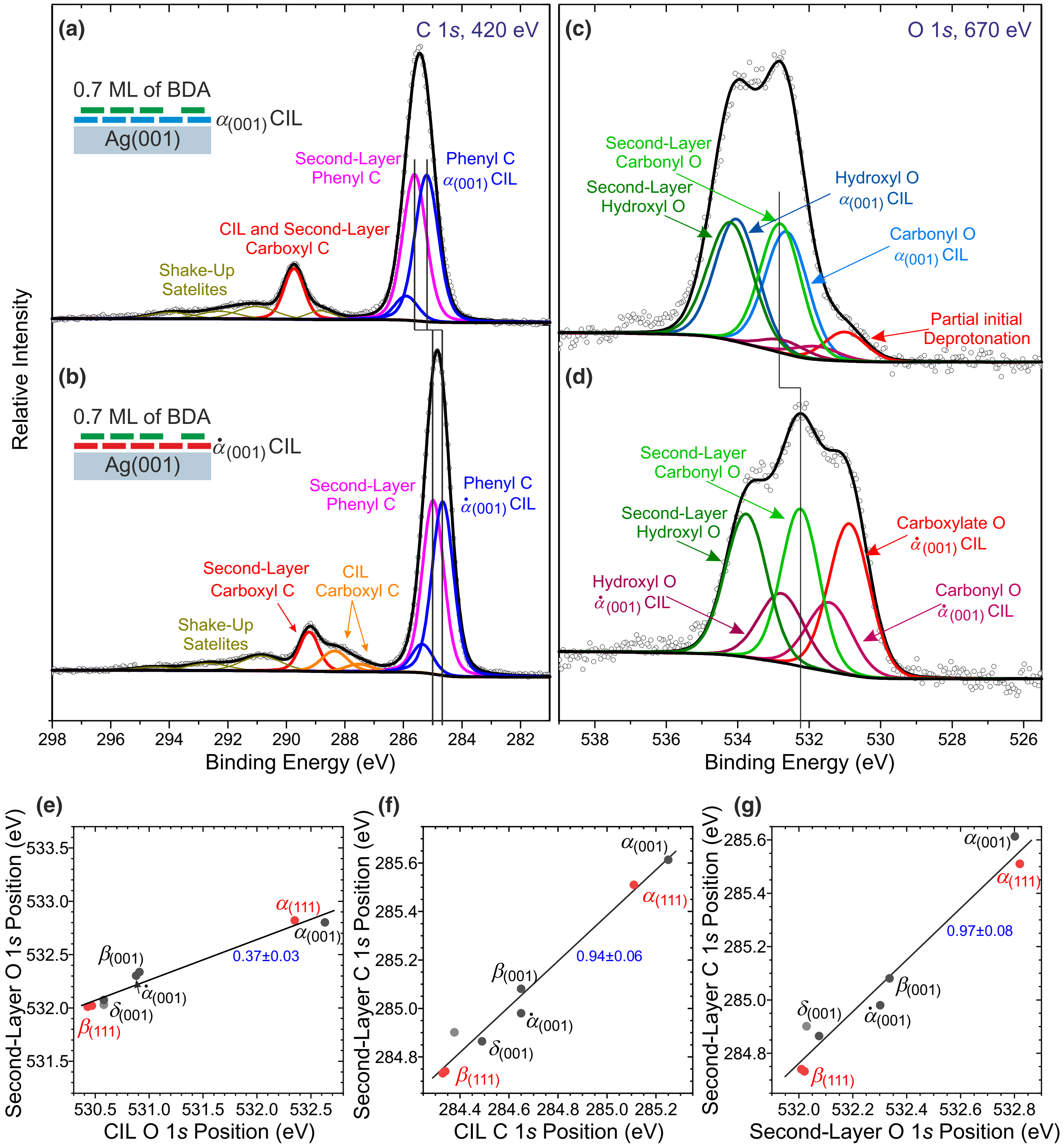

FIG. 6. Photoelectron-spectroscopy analysis of the second layer of BDA on the CILs. (a), (b) C 1*s* spectra measured by synchrotron radiation with an energy of 420 eV from samples comprising 0.7 ML of BDA deposited on the $\alpha_{(001)}$ and $\dot{\alpha}_{(001)}$ CILs, respectively. Peak components are marked accordingly. Full description and peak parameters are given in the Supplemental Material, Secs. 1 and 2 [38]. (c), (d) O 1*s* spectra (670 eV) of 0.7 ML of BDA deposited on the $\alpha_{(001)}$ and $\dot{\alpha}_{(001)}$ CILs, respectively. Vertical lines mark the shift of the peaks discussed in the text. Positions of the second-layer peaks as a function of the CIL carbonyl O 1*s* position (e), the CIL phenyl C 1*s* position (f), and the second-layer O 1*s* position (g). Gray point for the $\delta_{(001)}$ phase marks an incompletely formed layer. Energy scale is the same on both axes in each panel. Blue value denotes the slope of the linear fit (black line).

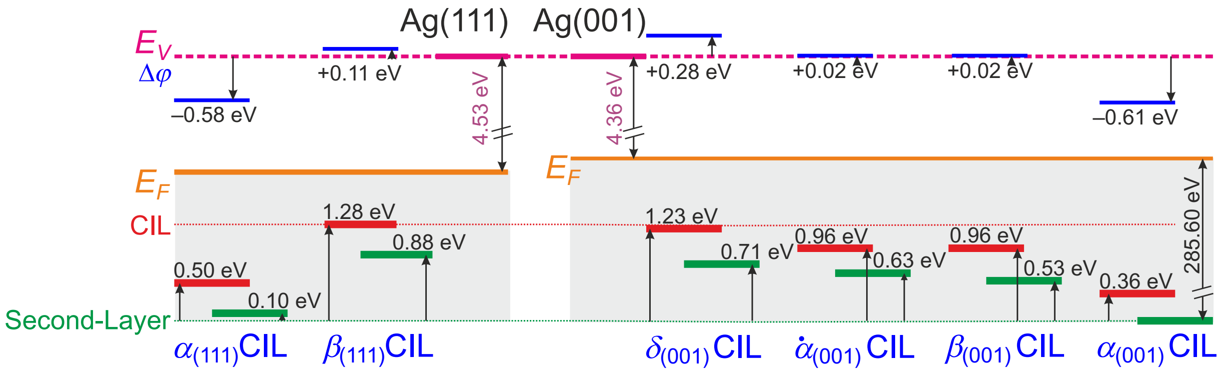

FIG. 7. Summary of energy-level positions determined for the studied CILs in an energy-level diagram; vacuum level, E_V; Fermi level, E_F; C 1*s* core-level positions of BDA in the CIL and the second layer; and WF shifts, $\Delta\varphi$, induced by the CILs are shown. Blue lines present the measured work functions with respect to the bare substrate (mean literature values [53] are taken for the substrate). Red and green lines mark the positions of the C 1*s* peak of BDA in the CILs (red lines) and second layers (green lines).

layer starts to desorb at 75 °C and disappears at 100 °C. Up to the desorption temperature, no changes in the peaks, except for a reduction in their intensity, are observed.

The C 1*s* spectrum of the $\alpha_{(001)}$ CIL [Fig. 2(a)] shows the phenyl-ring-associated component at 285.25 eV. After deposition of the BDA overlayer, the main peak significantly broadens. Taking the CIL spectra as a reference, a new component related to the second-layer C in the phenyl rings becomes apparent in Fig. 6(a). It has the same width and comparable intensity to those of the CIL peak but is shifted by 0.35 eV to higher BE. For the $\dot{\alpha}_{(001)}$ CIL, the spectrum in Fig. 6(b) is similar, but both the CIL and second-layer peaks are shifted to lower BEs compared to the $\alpha_{(001)}$ CIL: the CIL peak is at 284.65 eV, and the second-layer peak can be found at 0.35-eV-higher BE with respect to the CIL. Remarkably, for both the $\alpha_{(001)}$ and $\dot{\alpha}_{(001)}$ CILs, the shift of the second-layer peak relative to the CIL one is the same. The BDA C 1*s* core-level positions are summarized for all CILs in Fig. 7.

Figures 6(e) and 6(f) compare the energy shifts of the carbonyl O 1*s* and C 1*s* peaks in the second layer and the CIL. The O 1*s* peak components shift differently in the CIL and the second layer [Fig. 6(e)]. This indicates a strong interaction of carboxylate oxygens with the substrate [47], which is accompanied by a significant electronic transfer, as shown by our DFT calculations given in Sec. III A3. In contrast, the C 1*s* peak component associated with the phenyl rings shows a comparable shift in both the CIL and the second layer [Fig. 6(f); the slope is close to 1]. The rigid shift hints at the absence of the chemical interaction between C species and the substrate. Finally, Fig. 6(g) shows that the O 1*s* and C 1*s* peaks in the second BDA layer exhibit the same BE shift; this implies no chemical interaction of the second-layer molecules with all CILs. The position of the energy levels of the second-layer BDA in the valence-band region follows a similar trend: their shifts are consistent with the shifts of the core levels, as shown in the Supplemental Material, Sec. 4 [38]. The same shift of core and valence-band levels occurs when the molecular levels are aligned with the vacuum level [47,54]. In this case, we can employ the core-level shifts to probe local electric dipoles that are responsible for the ELA of frontier orbitals [13]. We note that, with an increasing overlayer thickness, the overlayer peaks shift towards the bulk values, as given in the Supplemental Material, Sec. 5 [38]; this behavior is probably a consequence of decreasing core-hole screening for ionized atoms at larger distances from the metal substrate [10,20,43]. The observed shifts in the second-layer energy levels in the range of 0.8 eV indicate that the considered BDA molecular phases can act as CILs.

C. Continuous tuning of energy-level alignment

Finally, we present a continuous tuning of the second-layer energy-level position, which is enabled by increasing the dipole density, n_{dip}, during the continuous isostructural phase transformation of $\alpha_{(001)}$ to the $\dot{\alpha}_{(001)}$ CIL [27]. This transition can be achieved by sample annealing at 70 °C [27] or by secondary electrons during exposure to x-ray radiation [41]. As the second-layer BDA already desorbs at 70 °C, the second option is favorable and enables simultaneous XPS analysis. The x-ray irradiation-induced deprotonation is restricted to the molecular layer that is in immediate contact with the Ag surface. Hence, in the case of 2 ML of BDA, only BDA molecules in the first layer slowly deprotonate ($\mathcal{D} \sim 0.5$ is reached in 42 h of irradiation) and n_{dip} continuously increases. Snapshots from the series of XPS spectra measured during irradiation are presented in Fig. 8. To evaluate the spectra, we use the peak parameters obtained from the pure phases described above and assume that the second-layer BDA does not chemically change during irradiation. This is substantiated by (i) the absence of deprotonation in the second layer

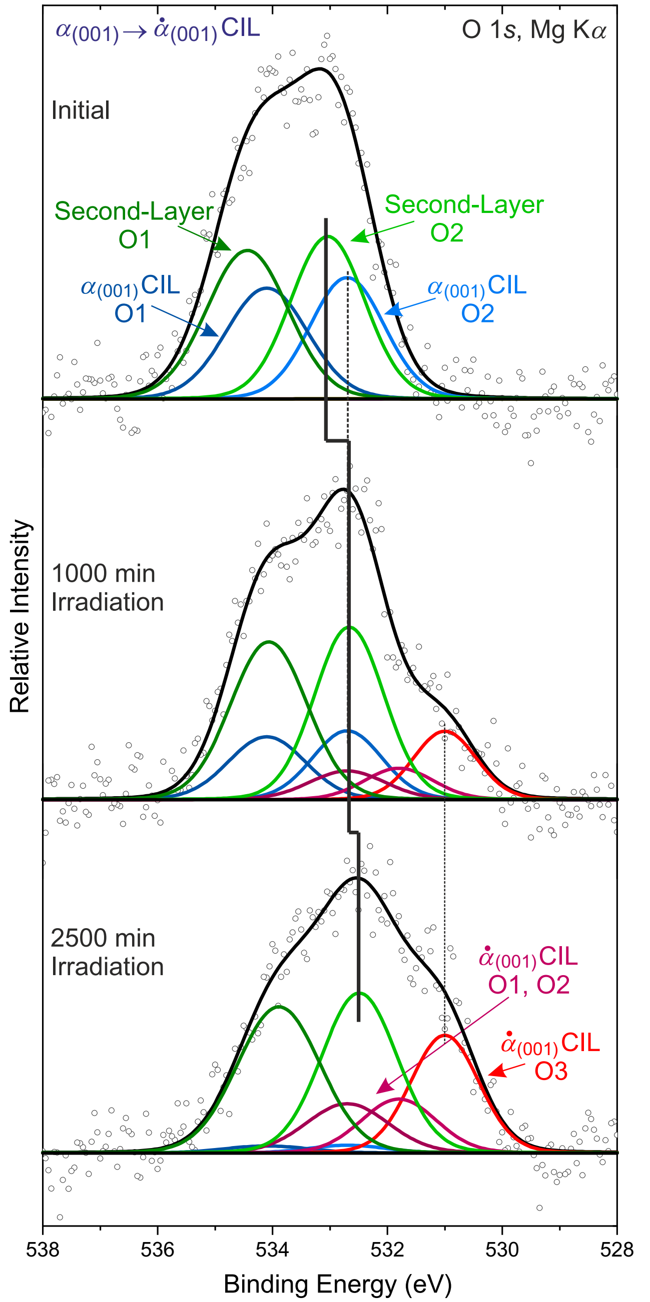

FIG. 8. Fitting of the O 1*s* XPS spectra measured during 2500-min-long x-ray exposure. Peaks associated with the $\alpha_{(001)}$ and $\dot{\alpha}_{(001)}$ CIL (the first layer) and the second layer are marked accordingly.

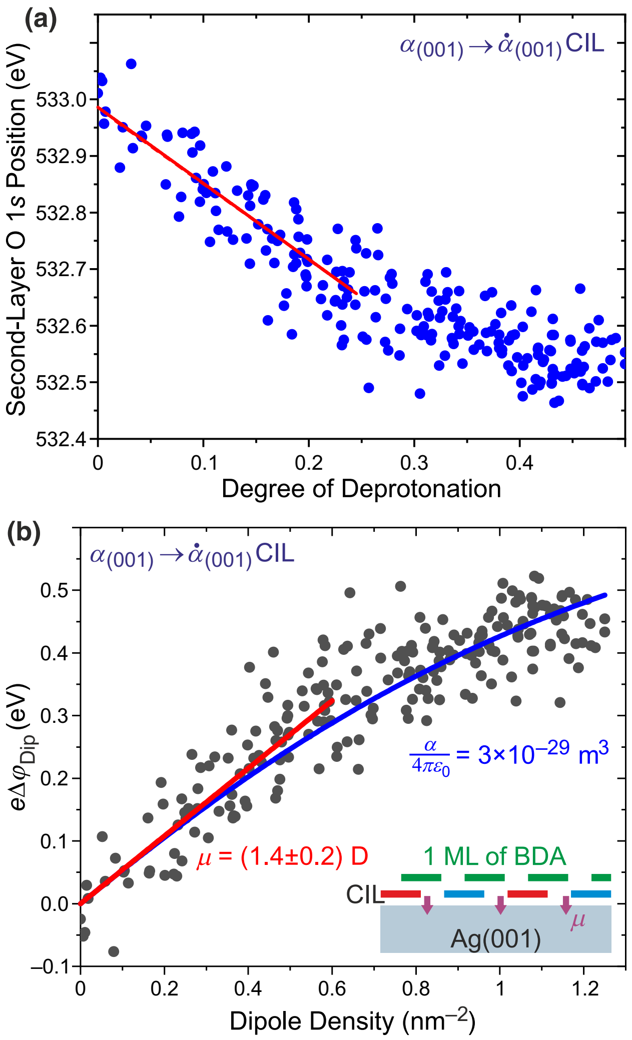

FIG. 9: (a) Shift of the second-layer O 1*s* peak as a function of the degree of deprotonation of the CIL. Variable degree of deprotonation is achieved during the isostructural $\alpha_{(001)}$ to $\dot{\alpha}_{(001)}$ transformation. (b) Work-function change determined from the shift of the second-layer O 1*s* peak as a function of electric dipole density, n_{dip}, during the isostructural $\alpha_{(001)}$ to $\dot{\alpha}_{(001)}$ transformation. Red line is a linear fit of the initial region, and blue curve is the full model given by Eq. (6).

on the $\delta_{(001)}$ CIL, even after annealing up to the desorption of the second layer, and (ii) the fact that bonding of the carboxylate to the substrate makes deprotonation energetically favorable. Therefore, we keep the intensity and Gaussian widths of the second-layer peaks constant during fitting of the whole series. The positions, intensity ratios, and Gaussian widths of individual components are kept constant for both CIL phases. The only free fitting parameters are the joint intensities of the α-phase CIL and the $\dot{\alpha}$-phase CIL peaks and position of the second-layer peaks. The degree of deprotonation is determined as the ratio of the carboxylate peak intensity to the total intensity of the first-layer (CIL) peaks.

The graph of the O 1*s* position as a function of $\mathcal{D}$ is given in Fig. 9(a). The second-layer energy-level position upshifts linearly by 0.4 eV for n_{dip} up to 0.6 nm^{-2} ($\mathcal{D} = 0.25$), beyond which it slows down: an additional shift by 0.1 eV is obtained for $n_{\mathrm{dip}} =$

$1.25\ \mathrm{nm}^{-2}$ ($\mathcal{D} = 0.5$). Figure 9(b) shows the work-function change determined from the shift of the second-layer O 1*s* peak as a function of the density of the interface dipoles that change from 0 to $1.25\ \mathrm{nm}^{-2}$. The shift in energy levels is given relative to the initial second-layer O 1*s* peak position of 532.99 eV. We note that, during synchrotron-radiation measurements, such damage is not observed because the sample is irradiated for much shorter times (~30 min) with a comparable photon flux. To confirm minimal beam damage, we occasionally shift the sample by a few millimeters and compared the spectra from fresh and long-illuminated spots; they look identical in all cases.

As discussed earlier, the upshift of electronic levels in the second layer is caused by the dipole component of the work-function change, $e\Delta\varphi_{\mathrm{dip}}$. In line with previous works on weakly interacting molecules that carry an electric dipole [49–51], the dependence of $e\Delta\varphi_{\mathrm{dip}}$ on n_{dip} can be approximated by the Topping model [44]. Assuming that the molecular dipoles are uniformly arranged and localized at a single point, the change in the work function can be expressed as

$$e\Delta\varphi_{\mathrm{dip}} = \frac{e}{\varepsilon_0}\mu n_{\mathrm{dip}}\left(1 + \frac{9\alpha}{4\pi\varepsilon_0}n_{\mathrm{dip}}^{3/2}\right)^{-1}, \tag{6}$$

where μ is the dipole moment, α is the polarizability of a surface-molecule complex, and ε_0 is the permittivity of vacuum. Modeling of the measured data is given in Fig. 9(b). The fit of the low-dipole-density part, in which it is sufficient to take only the linear part of Eq. (6), i.e., $(e/\varepsilon_0)\mu n_{\mathrm{dip}}$, gives the value of the electric dipole moment, $\mu = (1.4 \pm 0.2)$ D. Employing the value for the full model gives the polarizability volume, $\alpha/4\pi\varepsilon_0 = (3 \pm 1) \times 10^{-29}\ \mathrm{m}^3$; both values are consistent with those of similar systems [49,50]. Our DFT calculations give a value of dipole-moment change between the $\alpha_{(001)}$ and $\dot{\alpha}_{(001)}$ CILs of 1.2 D, in good agreement with the experimental value. Applying the model and derived values for the $\delta_{(001)}$ phase gives an energy shift of (0.64 ± 0.08) eV consistent with the measured value of 0.71 eV. The applicability of the model in Eq. (6) for the energy-level shifts in the second layer of deposited molecules shows that the change in the energy-level position in the BDA bilayer is caused by the dipolar contribution of the work-function change.

The properties presented above suggest that the layers of carboxylic acids can be used as tunable CILs. However, several issues have to be targeted before their application in devices. First, their favorable properties should be demonstrated on OSC layers. Second, the long-term stability of a deprotonation state in the carboxylic layers and the interaction of the layers under ambient conditions should be evaluated. With respect to the stability of a deprotonation state, our recent work shows that it is stabilized in specific molecular phases [29]. The other possibility is to design molecules possessing the required properties in the fully deprotonated state.

IV. CONCLUSIONS

We employ a single molecule to prepare a range of CILs on Ag(001) and Ag(111) surfaces by controlled deprotonation of the carboxylic groups, which results in the formation of interface dipoles with densities up to $2.3\ \mathrm{nm}^{-2}$. With an increasing density of dipoles, the sample's WF increases by up to 0.8 eV. We identify two distinct contributions to the formed dipoles: the interface dipoles increase the WF, whereas the intramolecular dipoles formed due to BDA molecule bending decrease the WF. The core energy levels of BDA molecules shift linearly with the WF change, as the dipoles electrostatically induce shifts in the kinetic energies of the photoelectrons. We demonstrate a continuous shift of energy levels of molecular overlayers in the range of 0 to 0.4 eV. This possibility makes the presented system a prospective candidate for the realization of efficient CILs in electronic devices featuring an OSC. The presented CILs feature flat-lying phenyl rings electronically strongly coupled to the metal substrate, which can serve as a favorable template for the growth of OSCs in the bulklike structure.

Data that support the findings of this study are available from the corresponding author upon reasonable request.

ACKNOWLEDGMENTS

This research is supported by GAČR, Project No. 22-04551S. We acknowledge CzechNanoLab Research Infrastructure (LM2018110) and e-INFRA CZ (ID:90140) supported by MEYS CR. The authors acknowledge the CERIC-ERIC Consortium for access to experimental facilities and financial support.

AUTHOR'S CONTRIBUTIONS

P.P. provided the initial idea. P.P. and J.Č. conceptualized the research. V.S. prepared the samples and performed all laboratory investigations. V.S., P.P., A.M., T.S., M.B., and J.Č. performed the synchrotron radiation experiments. J.P. and A.S. did DFT calculations. J.Č. developed the methodology, supervised the experiments, analyzed and interpreted data, and wrote the initial manuscript. All authors discussed the results and contributed to the final manuscript.

CONFLICT OF INTERESTS

The authors declare no competing financial interests.

DATA AVAILABILITY

The data that support the findings of this study are available from the corresponding author upon reasonable request.

[1] S. Zou, Y. Shen, F. Xie, J. Chen, Y. Li, and J.-X. Tang, Recent advances in organic light-emitting diodes: Toward smart lighting and displays, Mater. Chem. Front. **4**, 788 (2020).

[2] Y. Huang, E.-L. Hsiang, M.-Y. Deng, and S.-T. Wu, Mini-LED, Micro-LED and OLED displays: Present status and future perspectives, Light Sci. Appl. **9**, 105 (2020).

[3] S. Wang, H. Zhang, B. Zhang, Z. Xie, and W. Wong, Towards high-power-efficiency solution-processed OLEDs: Material and device perspectives, Mater. Sci. Eng., R **140**, 100547 (2020).

[4] S. K. Park, J. H. Kim, and S. Y. Park, Organic 2D optoelectronic crystals: Charge transport, emerging functions, and their design perspective, Adv. Mater. **30**, 1704759 (2018).

[5] J. Gao, J. Wang, C. Xu, Z. Hu, X. Ma, X. Zhang, L. Niu, J. Zhang, and F. Zhang, A critical review on efficient thick-film organic solar cells, Sol. RRL **4**, 2000364 (2020).

[6] Y. Yu, Q. Ma, H. Ling, W. Li, R. Ju, L. Bian, N. Shi, Y. Qian, M. Yi, L. Xie, and W. Huang, Small-molecule-based organic field-effect transistor for nonvolatile memory and artificial synapse, Adv. Funct. Mater. **29**, 1904602 (2019).

[7] M. Waldrip, O. D. Jurchescu, D. J. Gundlach, and E. G. Bittle, Contact resistance in organic field-effect transistors: Conquering the barrier, Adv. Funct. Mater. **30**, 1 (2020).

[8] H. Klauk, Will we see gigahertz organic transistors?, Adv. Electron. Mater. **4**, 1700474 (2018).

[9] N. Koch, Opportunities for energy level tuning at inorganic/organic semiconductor interfaces, Appl. Phys. Lett. **119**, 260501 (2021).

[10] A. Franco-Cañellas, S. Duhm, A. Gerlach, and F. Schreiber, Binding and electronic level alignment of π-conjugated systems on metals, Rep. Prog. Phys. **83**, 066501 (2020).

[11] R. Otero, A. L. Vázquez de Parga, and J. M. Gallego, Electronic, structural and chemical effects of charge-transfer at organic/inorganic interfaces, Surf. Sci. Rep. **72**, 105 (2017).

[12] M. Fahlman, S. Fabiano, V. Gueskine, D. Simon, M. Berggren, and X. Crispin, Interfaces in organic electronics, Nat. Rev. Mater. **4**, 627 (2019).

[13] E. Zojer, T. C. Taucher, and O. T. Hofmann, The impact of dipolar layers on the electronic properties of organic/inorganic hybrid interfaces, Adv. Mater. Interfaces **6**, 1900581 (2019).

[14] S. Braun, W. R. Salaneck, and M. Fahlman, Energy-level alignment at organic/metal and organic/organic interfaces, Adv. Mater. **21**, 1450 (2009).

[15] O. T. Hofmann, P. Rinke, M. Scheffler, and G. Heimel, Integer versus fractional charge transfer at metal(/insulator)/organic interfaces: Cu(/NaCl)/TCNE, ACS Nano **9**, 5391 (2015).

[16] M. P. Das and F. Green, in *AIP Conference Proceedings*, edited by S. M. Bose, S. N. Behera, and B. K. Roul (AIP, Bhubaneswar, India, 2008), Vol. 1063, pp. 26–34.

[17] H. Chen, W. Zhang, M. Li, G. He, and X. Guo, Interface engineering in organic field-effect transistors: Principles, applications, and perspectives, Chem. Rev. **120**, 2879 (2020).

[18] K.-G. Lim, S. Ahn, and T.-W. Lee, Energy level alignment of dipolar interface layer in organic and hybrid perovskite solar cells, J. Mater. Chem. C **6**, 2915 (2018).

[19] E. Goiri, P. Borghetti, A. El-Sayed, J. E. Ortega, and D. G. de Oteyza, Multi-component organic layers on metal substrates, Adv. Mater. **28**, 1340 (2016).

[20] J. L. Zhang, X. Ye, C. Gu, C. Han, S. Sun, L. Wang, and W. Chen, Non-covalent interaction controlled 2D organic semiconductor films: Molecular self-assembly, electronic and optical properties, and electronic devices, Surf. Sci. Rep. **75**, 100481 (2020).

[21] N. Koch, S. Duhm, J. P. Rabe, A. Vollmer, and R. L. Johnson, Optimized Hole Injection with Strong Electron Acceptors at Organic-Metal Interfaces, Phys. Rev. Lett. **95**, 237601 (2005).

[22] P. Borghetti, D. G. de Oteyza, C. Rogero, E. Goiri, A. Verdini, A. Cossaro, L. Floreano, and J. E. Ortega, Molecular-level realignment in donor–acceptor bilayer blends on metals, J. Phys. Chem. C **120**, 5997 (2016).

[23] R. Nouchi, M. Shigeno, N. Yamada, T. Nishino, K. Tanigaki, and M. Yamaguchi, Reversible switching of charge injection barriers at metal/organic-semiconductor contacts modified with structurally disordered molecular monolayers, Appl. Phys. Lett. **104**, 013308 (2014).

[24] P. Hurdax, M. Hollerer, P. Puschnig, D. Lüftner, L. Egger, M. G. Ramsey, and M. Sterrer, Controlling the charge transfer across thin dielectric interlayers, Adv. Mater. Interfaces **7**, 2000592 (2020).

[25] H. Edlbauer, E. Zojer, and O. T. Hofmann, Postadsorption work function tuning via hydrogen pressure control, J. Phys. Chem. C **119**, 27162 (2015).

[26] A. Kahn, Fermi level, work function and vacuum level, Mater. Horizons **3**, 7 (2016).

[27] P. Procházka, L. Kormoš, A. Shahsavar, V. Stará, A. O. Makoveev, T. Skála, M. Blatnik, and J. Čechal, Phase transformations in a complete monolayer of 4,4′-biphenyl-dicarboxylic acid on Ag(001), Appl. Surf. Sci. **547**, 149115 (2021).

[28] P. Procházka, M. A. Gosalvez, L. Kormoš, B. de la Torre, A. Gallardo, J. Alberdi-Rodriguez, T. Chutora, A. O. Makoveev, A. Shahsavar, A. Arnau, *et al.*, Multiscale analysis of phase transformations in self-assembled layers of 4,4′-biphenyl dicarboxylic acid on the Ag(001) surface, ACS Nano **14**, 7269 (2020).

[29] A. O. Makoveev, P. Procházka, M. Blatnik, L. Kormoš, T. Skála, and J. Čechal, Role of phase stabilization and surface orientation in 4,4′-biphenyl-dicarboxylic acid self-assembly and transformation on silver substrates, J. Phys. Chem. C **126**, 9989 (2022).

[30] L. Kormoš, P. Procházka, A. O. Makoveev, and J. Čechal, Complex K-uniform tilings by a simple bitopic precursor self-assembled on Ag(001) surface, Nat. Commun. **11**, 1856 (2020).

[31] G. Kresse and J. Furthmüller, Efficient iterative schemes for *ab initio* total-energy calculations using a plane-wave basis set, Phys. Rev. B **54**, 11169 (1996).

[32] G. Kresse and D. Joubert, From ultrasoft pseudopotentials to the projector augmented-wave method, Phys. Rev. B **59,** 1758 (1999).

[33] H. J. Monkhorst and J. D. Pack, Special points for Brillouin-zone integrations, Phys. Rev. B **13,** 5188 (1976).

[34] J. Klimeš, D. R. Bowler, and A. Michaelides, Chemical accuracy for the van der Waals density functional, J. Phys.: Condens. Matter **22,** 022201 (2010).

[35] S. Grimme, J. Antony, S. Ehrlich, and H. Krieg, A consistent and accurate *ab initio* parametrization of density functional dispersion correction (DFT-D) for the 94 elements H-Pu, J. Chem. Phys. **132,** 154104 (2010).

[36] J. Klimeš, D. R. Bowler, and A. Michaelides, van der Waals density functionals applied to solids, Phys. Rev. B **83,** 195131 (2011).

[37] J. MacLeod, Design and construction of on-surface molecular nanoarchitectures: Lessons and trends from trimesic acid and other small carboxylated building blocks, J. Phys. D **53,** 043002 (2020).

[38] See the Supplemental Material at http://link.aps.org/supplemental/10.1103/PhysRevApplied.18.044048 for an analysis of the photoelectron spectra of the BDA CILs on Ag(001), an analysis of the photoelectron spectra of the BDA CILs on Ag(111); work-function measurements of the CILs on Ag(001) and Ag(111) substrates, the mutual position of the valence and O 1*s* peaks in the second layer, and the position of the overlayer peaks as a function of the overlayer thickness.

[39] A. Schöll, Y. Zou, M. Jung, T. Schmidt, R. Fink, and E. Umbach, Line shapes and satellites in high-resolution x-ray photoelectron spectra of large π-conjugated organic molecules, J. Chem. Phys. **121,** 10260 (2004).

[40] M. Häming, A. Schöll, E. Umbach, and F. Reinert, Adsorbate-substrate charge transfer and electron-hole correlation at adsorbate/metal interfaces, Phys. Rev. B **85,** 235132 (2012).

[41] A. Makoveev, P. Procházka, A. Shahsavar, L. Kormoš, T. Krajňák, V. Stará, and J. Čechal, Kinetic control of self-assembly using a low-energy electron beam, Appl. Surf. Sci. **600,** 154106 (2022).

[42] T. Schultz, P. Amsalem, N. B. Kotadiya, T. Lenz, P. W. M. Blom, and N. Koch, Importance of substrate work function homogeneity for reliable ionization energy determination by photoelectron spectroscopy, Phys. Status Solidi **256,** 1800299 (2019).

[43] H. Ishii, K. Sugiyama, E. Ito, and K. Seki, Energy level alignment and interfacial electronic structures at organic/metal and organic/organic interfaces, Adv. Mater. **11,** 605 (1999).

[44] H. Lüth, *Solid Surfaces, Interfaces and Thin Films*, 6th ed. (Springer-Verlag Berlin Heidelberg, London, 2015).

[45] O. T. Hofmann, H. Glowatzki, C. Bürker, G. M. Rangger, B. Bröker, J. Niederhausen, T. Hosokai, I. Salzmann, R.-P. Blum, R. Rieger, *et al.*, Orientation-dependent work-function modification using substituted pyrene-based acceptors, J. Phys. Chem. C **121,** 24657 (2017).

[46] A. Franco-Cañellas, Q. Wang, K. Broch, D. A. Duncan, P. K. Thakur, L. Liu, S. Kera, A. Gerlach, S. Duhm, and F. Schreiber, Metal-organic interface functionalization via acceptor end groups: PTCDI on coinage metals, Phys. Rev. Mater. **1,** 013001(R) (2017).

[47] Q. Wang, A. Franco-Cañellas, P. Ji, C. Bürker, R.-B. Wang, K. Broch, P. K. Thakur, T.-L. Lee, H. Zhang, A. Gerlach, *et al.*, Bilayer formation vs molecular exchange in organic heterostructures: Strong impact of subtle changes in molecular structure, J. Phys. Chem. C **122,** 9480 (2018).

[48] S. Kera, Y. Yabuuchi, H. Yamane, H. Setoyama, K. K. Okudaira, A. Kahn, and N. Ueno, Impact of an interface dipole layer on molecular level alignment at an organic-conductor interface studied by ultraviolet photoemission spectroscopy, Phys. Rev. B **70,** 085304 (2004).

[49] H. Fukagawa, H. Yamane, S. Kera, K. K. Okudaira, and N. Ueno, Experimental estimation of the electric dipole moment and polarizability of titanyl phthalocyanine using ultraviolet photoelectron spectroscopy, Phys. Rev. B **73,** 041302(R) (2006).

[50] H. Fukagawa, S. Hosoumi, H. Yamane, S. Kera, and N. Ueno, Dielectric properties of polar-phthalocyanine monolayer systems with repulsive dipole interaction, Phys. Rev. B **83,** 085304 (2011).

[51] A. Gerlach, T. Hosokai, S. Duhm, S. Kera, O. T. Hofmann, E. Zojer, J. Zegenhagen, and F. Schreiber, Orientational Ordering of Nonplanar Phthalocyanines on Cu(111): Strength and Orientation of the Electric Dipole Moment, Phys. Rev. Lett. **106,** 156102 (2011).

[52] M. Häming, M. Greif, C. Sauer, A. Schöll, and F. Reinert, Electronic structure of ultrathin heteromolecular organic-metal interfaces: SnPc/PTCDA/Ag(111) and SnPc/Ag(111), Phys. Rev. B **82,** 235432 (2010).

[53] G. N. Derry, M. E. Kern, and E. H. Worth, Recommended values of clean metal surface work functions, J. Vac. Sci. Technol., A **33,** 060801 (2015).

[54] A. El-Sayed, P. Borghetti, E. Goiri, C. Rogero, L. Floreano, G. Lovat, D. J. Mowbray, J. L. Cabellos, Y. Wakayama, A. Rubio, *et al.*, Understanding energy-level alignment in donor–acceptor/metal interfaces from core-level shifts, ACS Nano **7,** 6914 (2013).